



# Tungsten diselenide/porous carbon with sufficient active edge-sites as a co-catalyst/Pt-support favoring excellent tolerance to methanol-crossover for oxygen reduction reaction in acidic medium



Siyu Pan <sup>a,b</sup>, Zhuang Cai <sup>a</sup>, Yaqiang Duan <sup>a,b</sup>, Liu Yang <sup>a,b</sup>, Bo Tang <sup>a,b</sup>, Baojian Jing <sup>a,b</sup>, Ying Dai <sup>a,c,\*</sup>, Xin Xu <sup>a,b</sup>, Jinlong Zou <sup>a,b,\*</sup>

<sup>a</sup> Key Laboratory of Functional Inorganic Material Chemistry, Ministry of Education of the People's Republic of China, School of Chemistry and Materials Science, Heilongjiang University, Harbin, 150080, China

<sup>b</sup> Key Laboratory of Chemical Engineering Process and Technology for High-Efficiency Conversion, College of Heilongjiang Province, Heilongjiang University, Harbin, 150080, China

<sup>c</sup> School of Civil Engineering, Heilongjiang Institute of Technology, Harbin 150050, China

## ARTICLE INFO

### Article history:

Received 20 April 2017

Received in revised form 8 June 2017

Accepted 5 July 2017

Available online 14 July 2017

### Keywords:

Tungsten diselenide  
Direct methanol fuel cells  
Durability  
Oxygen reduction reaction  
Methanol tolerance

## ABSTRACT

Developing an acid-stable, highly active and methanol-tolerant electrocatalyst towards the oxygen reduction reaction (ORR) is crucial for commercialization of direct methanol fuel cells (DMFCs). In this study, via a simultaneous synthesis method, tungsten diselenide/porous carbon (WSe<sub>2</sub>/C) composites are prepared as the supports/ORR co-catalysts to support Pt with a low loading of 5 wt.%. Varied WSe<sub>2</sub>/C supports are obtained by tuning the carbonization temperature (600–1000 °C) to investigate the relationships between structural characteristics and ORR performance. Pt-WSe<sub>2</sub>/C (800 °C) exhibits a considerably higher specific activity (4.57 mA cm<sup>-2</sup>) for ORR than those of WSe<sub>2</sub>/C (2.45 mA cm<sup>-2</sup>) and commercial Pt/C (10 wt.%, 2.69 mA cm<sup>-2</sup>), owing to the high ORR co-catalytic activity of WSe<sub>2</sub>/C for Pt. The robust contacts among Pt, WSe<sub>2</sub> and porous carbon with high surface area can significantly improve the exposure of Pt active sites, which correspondingly promote the charge transfer efficiency and the fast adsorption, activation and reduction of oxygen molecules. Moreover, Pt-WSe<sub>2</sub>/C (800 °C) catalyst exclusively exhibits a four-electron pathway for ORR. With the intimate cooperation among Pt, WSe<sub>2</sub> and porous carbon skeleton, more available Pt active sites are exposed to improve the ORR kinetics and durability. The tolerance to methanol-crossover on Pt-WSe<sub>2</sub>/C are remarkably enhanced, which should be attributed to the synergistic effects between the exposed edge sites of embedded WSe<sub>2</sub> and the porous carbon skeleton with abundant oxygen-containing functional groups. The use of WSe<sub>2</sub>/C supports with low-cost, high co-catalytic/catalytic activity and strong methanol-tolerance provides a promising way to enhance ORR activity in DMFCs.

© 2017 Elsevier B.V. All rights reserved.

## 1. Introduction

With the globalization of energy crisis and the severity of environmental pollution, the development of new clean energy is of great importance and high priority, especially for China. Direct methanol fuel cells (DMFCs) as the promising and environmental-friendly energy generation systems, which can convert chemical energy of methanol fuel directly into electrical energy, have been attracted more and more attention [1]. Although the great achieve-

ments have been made in recent years, there are still several major issues that affect the conversion efficiency and power density of DMFCs. One of the main problems is the methanol crossover, which means that methanol molecules cross over from the anode to the cathode through the polymer electrolyte membrane and then are oxidized at the cathode catalyst layer to cause the decrease of the cathodic potential, resulting in a loss of fuel efficiency [2–4]. Furthermore, the high cost, scarcity of precious metal resources and poor durability of cathode catalysts are also the main obstacles to the commercialization of DMFCs. Therefore, it is urgent to explore a high-efficiency cathode catalyst with relatively low cost, which not only has high activity for oxygen reduction reaction (ORR), but also exhibits good durability and strong tolerance against methanol crossover [5,6].

\* Corresponding authors at: Xuefu Road 74, Nangang District, Harbin, 150080, China.

E-mail addresses: [zjh\\_0308@126.com](mailto:zjh_0308@126.com) (Y. Dai), [zoujinlong@aliyun.com](mailto:zoujinlong@aliyun.com) (J. Zou).

Recently, several attempts have been proposed to investigate the methanol-tolerant ORR catalysts without platinum (Pt) usage, such as metal chalcogenides [7,8], transition metal oxides [9,10], Co, Fe and Ni containing organic macrocycles [11–13], Ru chalcogenides and RuSe<sub>y</sub> compound catalysts [14,15], which have shown the high tolerance to methanol in fuel cell tests. However, their ORR activities are still much lower than that of Pt-based catalysts, especially in methanol-free electrolytes. Hence, it is still difficult to achieve the commercial application of DMFCs by only relying on non-Pt materials. Therefore, reducing the amount of Pt loading in catalysts has become the focus of this field. Several strategies are developed to prepare Pt alloyed electrocatalysts with transition metals such as Pt-Fe [16], Pt-Co [17], Pt-Cu [18], Pt-Ni [19], Pt-Cr [20], or to deposit a Pt monolayer onto other nanoparticles [21,22]. These materials are employed to improve both the electrocatalytic activity in ORR and the tolerance towards methanol crossover.

In addition, developing the novel carbon supports to promote the performance of the electrocatalysts has also attracted much more attention [23]. The carbon materials, with a sequential structure and high electrical conductivity, can dramatically improve the performance of Pt-based catalysts [24–27]. The usually-used carbon materials including carbon nanotubes (CNTs), carbon nanofibers (CNFs), carbon nanocoils, ordered mesoporous carbons (OMCs) and graphene have already been investigated as catalyst supports [24–27]. It is reported that ORR activity and methanol tolerance of OMCs-supported Pt-Fe catalyst prepared by the nanocasting method have been improved [16]. Song et al. synthesize the carbon-coated graphene/Pt catalysts by using a two-step method, which exhibits high ORR performance and methanol tolerance because of the presence of the protective carbon layer on Pt surface [28]. Furthermore, the long-term ORR durability is greatly improved by the strong interactions between Pt nanoparticles and graphene through electron delocalization [28]. However, the Pt/carbon catalysts still show some shortcomings for ORR and therefore the non-metals (N, S, Se, etc) doped carbon-supported Pt catalysts are further studied [29]. Wang et al. prepare the Pt-Se/C catalyst by a modified organic colloidal approach [29]. The doping of Se in the carbon skeleton (Vulcan XC-72R) can significantly improve the dispersion of active Pt components, which thus improve the ORR activity and methanol tolerance [29].

In recent years, the transition-metal compounds have been used as co-catalysts and/or catalyst supports, which have already exhibited high activity and Pt utilization for ORR [6]. Among these catalysts, transition-metal selenides have been used as electro-catalysts in many fields including electro-catalysis [11,30], hydrogen evolution reaction (HER) [31,32], fuel cells [33], etc. Tungsten diselenide (WSe<sub>2</sub>) has been tested as a promising one to substitute Pt catalyst for HER [31,32,34]. In particular, WSe<sub>2</sub> with a structure composed of three stacked atom layers (Se–W–Se) bonded together by van der Waals forces, has been shown to be a promising material for catalysis [34]. The electrocatalytic properties of WSe<sub>2</sub> greatly depend on its exposed edge sites and electrical conductivity [35]. It is also reported that the carbon-supported WSe<sub>2</sub> can be used as active catalysts for HER, exhibiting excellent activity and stability due to their high conductivity and low onset over-potential [36]. Wang et al. investigate the activity of CNTs-supported WSe<sub>2</sub> catalysts, which are prepared by the one-pot solvothermal reaction method [36]. The excellent catalytic performance of the WSe<sub>2</sub>/CNTs for HER is attributed to the increased number of catalytic active sites and enhanced charge transfer kinetics due to the intimate contacts between the catalytic WSe<sub>2</sub> nanosheets and the highly conductive CNT skeleton [36]. However, until now, WSe<sub>2</sub> is rarely investigated as the co-catalyst and/or support for ORR, which is quite different from HER catalysis, deserving further study to clarify the ORR property and mechanisms, especially in acidic medium.

In this study, for the first time, WSe<sub>2</sub>/porous carbon (WSe<sub>2</sub>/C) composites are prepared as Pt supports and ORR co-catalysts via a simultaneous synthesis method. After carbonization, citric acid (CiA) as the carbon source is converted into porous carbon, meanwhile WSe<sub>2</sub> nanoparticles are in situ embedded in the carbon skeleton, which are intimately incorporated with the carbon phase, thus increasing the number of the exposed edge sites. Pt nanoparticles are supposed to be well-dispersed on the porous structure of WSe<sub>2</sub>/C, which can facilitate the exposure of more Pt active sites and the charge transfer kinetics. Compared with individual WSe<sub>2</sub>/C and Pt/C, the catalytic activity of Pt-WSe<sub>2</sub>/C for ORR is expected to be considerably improved in both methanol and methanol-free electrolytes. It is also expected that Pt-WSe<sub>2</sub>/C catalysts should exhibit a much higher tolerance to methanol poisoning (methanol crossover) than that of commercial Pt/C under the same condition and can overcome the loss/deterioration of ORR activity and durability with methanol.

## 2. Experimental

### 2.1. Synthesis of WSe<sub>2</sub>/C composites

In a typical preparation procedure, 0.8 g of selenium powder was dispersed in 8 mL of hydrazine hydrate at 80 °C via 1 h stirring to obtain the Se-containing solution. Meanwhile, 3.3 g of CiA and 1 g of (NH<sub>4</sub>)<sub>10</sub>H<sub>2</sub>(W<sub>2</sub>O<sub>7</sub>)<sub>6</sub> were dissolved in deionized water, which was then added to the Se-containing solution under vigorous stirring. The mixture was continuously stirred in a water bath at 80 °C for 10 h. Then it was dried at 100 °C in an oven to completely remove the water. After that, the ground precursor was carbonized from room temperature to 600, 700, 800, 900 and 1000 °C (5 °C min<sup>-1</sup>) in flowing nitrogen (N<sub>2</sub>) atmosphere (50–60 mL min<sup>-1</sup>). The precursor was soaked at the final temperature for 2 h, followed by naturally cooling to room temperature under the N<sub>2</sub> gas flowing. The final samples were marked as WSe<sub>2</sub>/C-x (x = 600, 700, 800, 900 and 1000).

### 2.2. Synthesis of Pt-WSe<sub>2</sub>/C composites

Pt-WSe<sub>2</sub>/C composites with a nominal Pt loading of 5 wt.% were prepared by using the modified borohydride reduction method. 100 mg of WSe<sub>2</sub>/C-x composites was placed in a mortar, meanwhile, H<sub>2</sub>PtCl<sub>6</sub>•6H<sub>2</sub>O aqueous solution with Pt<sup>2+</sup> concentration of 2 mM was slowly added into the mortar. Then, it was dried at 80 °C in an oven to completely remove the water. Excessive sodium borohydride was added to the dried products for 2 h grinding. Finally, the obtained precursors were carbonized from room temperature to 350 °C (1 °C min<sup>-1</sup>) in flowing nitrogen (N<sub>2</sub>) atmosphere. The precursors were soaked at 350 °C for 40 min, followed by naturally cooling to room temperature under the N<sub>2</sub> gas (50–60 mL min<sup>-1</sup>). The final Pt-WSe<sub>2</sub>/C samples were washed with distilled water and ethanol to remove the residual sodium borohydride.

### 2.3. Materials characterization

X-ray diffraction (XRD) patterns were recorded on a Rigaku D/max 2500 diffractometer using Cu K $\alpha$  radiation ( $\lambda$  = 1.5406 Å, 40 kV, 20 mA) at step scan of 0.02°. Scanning electron microscopy (SEM) images were taken using an S-4800 scanning electron microscope (Japan) with an accelerating voltage of 5.0 kV. Transmission electron microscopy (TEM) and high-resolution TEM (HRTEM) images were obtained using a JEM-2100 electron microscope (JEOL) with an acceleration voltage of 200 kV. N<sub>2</sub> adsorption/desorption isotherms were measured using a Tristar II 3020 Micromeritics adsorption analyzer at 77 K. Specific surface areas and pore

size distributions (PSD) were calculated by using the Brunauer–Emmett–Teller (BET) theory and the Barrett–Joyner–Halenda (BJH) method, respectively. Total pore volume was estimated from the adsorption volume at a relative pressure ( $P/P_0$ ) of 0.98. X-ray photoelectron spectroscopy (XPS) spectra were acquired on a Kratos-AXISUL TRA DLD X-ray photoelectron spectrometer with Al K $\alpha$  as the excitation source. It was used to analyze the surface components of the catalysts by deconvolution of C 1s, O 1s, W 4f, Se 3d and Pt 4f spectra.

#### 2.4. Electrochemical measurements

5 mg of Pt-WSe<sub>2</sub>/C was dispersed in a mixture of solvents containing 100  $\mu$ L of ethanol and 50  $\mu$ L of Nafion solution to form a suspension, which was then dispersed in an ultrasonic bath for 15 min to obtain the homogeneous ink [37]. 10 wt.% of commercial Pt/C was used as the control sample. A glassy carbon (GC) disk electrode with diameter of 3 mm and area of 0.07065 cm<sup>2</sup> was used. Prior to each use, the GC electrode was polished with Al<sub>2</sub>O<sub>3</sub> slurry and washed with deionized water and ethanol. Electrocatalytic activity was evaluated via the cyclic voltammetry (CV) and the rotating disk electrode (RDE) techniques. Electrochemical measurements were performed in a standard three-electrode glass cell on a CHI 760E electrochemical workstation (Chenhua, Shanghai) under ambient conditions. The catalyst ink (5  $\mu$ L) was gradually dropped onto the electrode and naturally dried under ambient conditions. The GC electrode, 1 cm<sup>2</sup> Pt plate, and saturated calomel electrode (SCE, +0.2415 V vs standard hydrogen electrode, 3.0 M KCl) were used as the working, counter, and reference electrodes, respectively. Aqueous solution of 0.5 M H<sub>2</sub>SO<sub>4</sub> with or without methanol was used as the electrolytes. CV tests were conducted from −0.2 to 1.0 V at a scan rate of 10 mV s<sup>−1</sup> with a continuous O<sub>2</sub> flow. Electrochemical impedance spectroscopy (EIS) and chronoamperometry (CA) and tafel tests were conducted in a self-assembled three electrode cell at a rotation rate of 1600 rpm by using the same methods as previously reported [33,36].

The RDE measurements were conducted in O<sub>2</sub>-saturated H<sub>2</sub>SO<sub>4</sub> with or without methanol solution at a scan rate of 5 mV s<sup>−1</sup> and various rotation speeds from 400 to 2500 rpm. Koutecky–Levich (K-L) plots ( $J^{-1}$  vs.  $\omega^{-1/2}$ ) were obtained at the potentials of 0.15–0.30 V, which were fitted into the linear curves to calculate the electron transfer numbers (n) by using the K-L equation [33,38]:

$$\frac{1}{J} = \frac{1}{J_K} + \frac{1}{B\omega^{1/2}}$$

Where  $J$  is the measured current density (mA cm<sup>−2</sup>),  $J_K$  is the kinetic current density, and  $\omega$  is the rotating rate (rpm).  $B$  is calculated from the slope of K-L plots on the basis of the following equation:

$$B = 0.2nFC_0D_0^{2/3}\nu^{-1/6}$$

Where  $n$  is the number of electrons transferred per oxygen molecule,  $F$  is the Faraday constant (96485 C mol<sup>−1</sup>),  $C_0$  is the bulk concentration of O<sub>2</sub> ( $1.2 \times 10^{-6}$  mol cm<sup>−3</sup>),  $D_0$  is the O<sub>2</sub> diffusion coefficient ( $1.9 \times 10^{-5}$  cm<sup>2</sup> s<sup>−1</sup>), and  $\nu$  is the kinematic viscosity of the electrolyte (0.01 cm<sup>2</sup> s<sup>−1</sup>). The constant of 0.2 is adopted when the rotation speed is expressed in rpm.

### 3. Results and discussion

#### 3.1. Characteristics and structure of WSe<sub>2</sub>/C and Pt-WSe<sub>2</sub>/C composites

Fig. 1 shows the XRD patterns of the WSe<sub>2</sub>/C composites and Pt-WSe<sub>2</sub>/C catalysts obtained at different temperatures. As shown

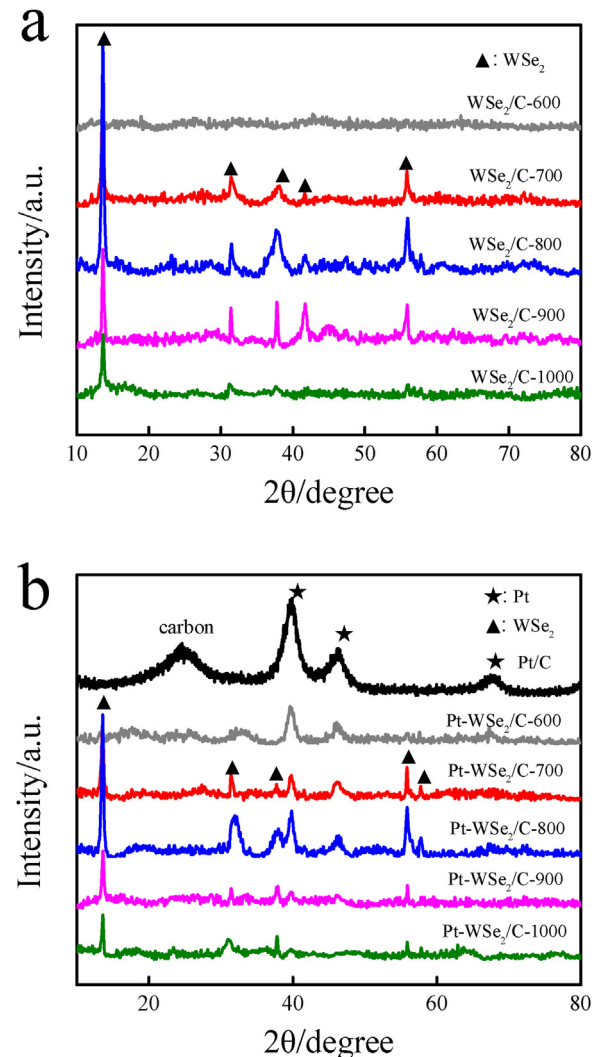


Fig. 1. XRD patterns of WSe<sub>2</sub>/C (a) and Pt-WSe<sub>2</sub>/C (b) composites.

in Fig. 1a, all of the synthesized WSe<sub>2</sub>/C-x ( $x=700, 800, 900$  and  $1000$ ) without WSe<sub>2</sub>/C-600 show the typical crystalline phase of WSe<sub>2</sub>. The diffraction peaks at  $13.6^\circ$ ,  $31.4^\circ$ ,  $37.8^\circ$ ,  $41.7^\circ$ ,  $55.9^\circ$  are assigned to the (002), (100), (103), (006) and (110) crystalline planes of WSe<sub>2</sub>, respectively (No. 38-1388, JCPDS) [33,36]. Generally, the structure of each WSe<sub>2</sub> cells is composed of three stacked atom layers (Se–W–Se) [34]. Apparently, the WSe<sub>2</sub> peak densities of WSe<sub>2</sub>/C-800 and WSe<sub>2</sub>/C-900 are stronger than those of other WSe<sub>2</sub>/C composites and no peaks of WSe<sub>2</sub> can be observed at  $600^\circ\text{C}$ , indicating that carbonization temperature is crucial for enhancing the crystallinity and stability of WSe<sub>2</sub>. As shown in Fig. 1b, the XRD patterns clearly show the characteristic peaks of the face-centered cubic (fcc) crystalline Pt at  $39.8^\circ$  and  $46.2^\circ$ , which correspond to the Pt (111) and Pt (200) planes, respectively (No. 65-2868, JCPDS) [16,28]. The peaks of (103) and (006) planes of WSe<sub>2</sub> cannot be observed in XRD patterns due to the strong peak intensity of Pt (111). Moreover, no graphite peak can be detected at around  $26^\circ$  in Fig. 1b, indicating that most of the carbon skeleton in WSe<sub>2</sub>/C composites are amorphous. This result is also confirmed by the following SEM and TEM images (Fig. 4).

N<sub>2</sub> adsorption/desorption isotherms are measured to investigate the pore structure of WSe<sub>2</sub>/C-x ( $x=600, 700, 800, 900$  and  $1000$ ) composites. The isotherms of all of the as-synthesized composites are the type-IV pattern with a distinct hysteresis loop at relative pressures ( $P/P_0$ ) from 0.4 to 0.8 (Fig. S1), suggesting the

**Table 1**Binding energies and surface compositions for Pt 4f core level region of Pt-WSe<sub>2</sub>/C-x.

Samples	Pt (0)		Pt (II)		Pt (IV)	
	Binding energy (eV)	Relative ratio (%)	Binding energy (eV)	Relative ratio (%)	Binding energy (eV)	Relative ratio (%)
Pt-WSe <sub>2</sub> /C-600	71.2	42.8	72.6	32.2	73.7	25.1
	74.9		76.3		77.5	
Pt-WSe <sub>2</sub> /C-700	71.5	46.1	72.7	35.5	74.2	18.4
	75.1		76.3		77.8	
Pt-WSe <sub>2</sub> /C-800	71.5	49.6	72.8	38.3	74.1	12.1
	75.0		76.3		77.4	
Pt-WSe <sub>2</sub> /C-900	71.8	53.6	72.8	32.4	73.8	14.0
	75.1		76.2		77.2	
Pt-WSe <sub>2</sub> /C-1000	71.7	56.3	72.7	30.5	73.6	13.2
	75.1		76.3		77.6	
10 wt.% Pt/C	71.9	44.2	73.3	20.1	75.2	35.7
	76.5		77.8		79.2	

presence of mesopores in these materials [33]. The PSD curves of all of the samples are centered at approximately 2–50 nm, confirming the mesoporous nature of these composites [33]. Moreover, as shown in Table 1, the larger BET surface areas ( $S_{BET}$ ) are obtained by WSe<sub>2</sub>/C-800 and WSe<sub>2</sub>/C-900, which are 86.34 and 77.70 m<sup>2</sup> g<sup>-1</sup>, respectively. The higher pore volumes are also obtained by WSe<sub>2</sub>/C-800 (0.05 cm<sup>3</sup> g<sup>-1</sup>) and WSe<sub>2</sub>/C-900 (0.04 cm<sup>3</sup> g<sup>-1</sup>), as presented in Table S1. The relatively large surface areas of the as-prepared carbon-supported WSe<sub>2</sub> can provide more exposed edge sites of WSe<sub>2</sub> to facilitate the transport, adsorption and activation of oxygen molecules during the ORR. Furthermore, the WSe<sub>2</sub>/C composites with porous structure can offer sufficient active sites to support/bind Pt nanoparticles and provide enough promising functional groups to improve their co-catalytic activity.

The surface elemental compositions of the Pt-WSe<sub>2</sub>/C catalysts are investigated through XPS tests. The XPS survey spectra of Pt-WSe<sub>2</sub>/C-x ( $x = 600, 700, 800, 900$  and 1000) are shown in Fig. 2a. The spectra indicate the presence of Pt, W, Se, C and O for Pt-WSe<sub>2</sub>/C. The predominant peaks centered at around 284.6 and 532.0 eV refer to the C 1s and O 1s, respectively [33,36]. The peaks of W 4f and Se 3d locate at around 32.1 and 54.6 eV, respectively [31,33,34]. The Pt 4f peaks at around 71.6 eV are also observed in the spectra, which confirm that the metallic Pt species are successfully deposited onto the WSe<sub>2</sub>/C supports [5].

The high-resolution XPS spectra of Pt 4f for Pt-WSe<sub>2</sub>/C-x ( $x = 600, 700, 800, 900$  and 1000) are presented in Fig. 2b and Fig. S2. The Pt 4f spectra can be divided into three pairs of doublets, which can be attributed to the different valence states of Pt [5,28,29]. In Fig. 2b, the most intense doublet (at around 71.5 and 75.0 eV) corresponds to the metallic Pt (Pt (0)) [5]. The weaker doublet (at around 72.8 and 76.3 eV) can be assigned to the oxidation state of Pt in the form of PtO [28]. The weakest doublet (at around 74.1 and 77.4 eV) should correspond to the PtO<sub>2</sub> [29]. Moreover, the binding energies of the metallic Pt 4f of Pt-WSe<sub>2</sub>/C catalysts have negative shifts of 1.4–1.6 eV in comparison with that of commercial Pt/C. The shift of Pt (0) peak to a lower binding energy means that less PtO<sub>x</sub> species originating from the oxidation of the finely-dispersed Pt (0) particles are existed on the surface of WSe<sub>2</sub>/C, which can be attributed to the change in Pt oxidation state caused by the strong Pt-WSe<sub>2</sub> and/or Pt-carbon interactions effects [39–41]. The Pt (0) proportions of Pt-WSe<sub>2</sub>/C-x ( $x = 700, 800, 900$  and 1000) are higher than that of Pt/C, implying that WSe<sub>2</sub>/C supports/co-catalysts can offer more binding sites to stabilize Pt (0) to provide more available Pt active sites for ORR (Table 1). Moreover, compared to the Pt (0) with high corrosion resistance, PtO<sub>x</sub> species are relatively unstable in the electrochemical environment and easily re-deposited onto the support by reductants, resulting in the re-growth (aggregation) of Pt nanoparticles and the loss of electroactive Pt surface areas [28]. Therefore, the higher content of Pt (0) species and the lower con-

tent of PtO<sub>x</sub> species on Pt-WSe<sub>2</sub>/C are crucial to improve the cycling performance of the catalysts [28,42].

As shown in Fig. 2c and Fig. S3, the W 4f spectra of Pt-WSe<sub>2</sub>/C-x ( $x = 600, 700, 800, 900$  and 1000) can be decomposed into two pairs of doublets. The peaks of W 4f<sub>7/2</sub> and W 4f<sub>5/2</sub> locate at around 32.1 and 34.2 eV, respectively, corresponding to the +4 oxidation chemical state of W [31,33]. The peaks at around 35.5 and 37.8 eV are assigned to W 4f<sub>7/2</sub> and W 4f<sub>5/2</sub>, respectively, which correspond to the +6 oxidation state of surface W originating from the formation of a small amount of WO<sub>3</sub> under the air exposure condition [31,33]. No metallic W (0) peak at around 31.4 eV can be found for Pt-WSe<sub>2</sub>/C, implying that expect for the formation of WO<sub>3</sub>, W is mainly bound with Se to form WSe<sub>2</sub> in the carbon skeleton. Fig. 2d and Fig. S4 show the Se 3d binding energy regions for Pt-WSe<sub>2</sub>/C. The peaks at around 54.3 and 55.2 eV correspond to the Se 3d<sub>5/2</sub> and Se 3d<sub>3/2</sub>, respectively, confirming the valence state of -2 for Se in WSe<sub>2</sub> [31,33,34]. In addition, the atomic ratios of Se/W of Pt-WSe<sub>2</sub>/C-x ( $x = 700, 800, 900$  and 1000) are in the range of 1.7: 1–2.8: 1, which are close to the theoretical atomic ratio (2: 1) of WSe<sub>2</sub>. The well crystallized WSe<sub>2</sub> embedded in carbon skeleton can increase the number of active binding-sites for anchoring Pt and improve the electrical conductivity to provide easy transfer charge ability. Note that the atomic ratio of Se/W of Pt-WSe<sub>2</sub>/C-600 is 20: 1, implying that the WSe<sub>2</sub> is not synthesized at 600 °C, consistent with the XRD result.

The C 1s spectra of Pt-WSe<sub>2</sub>/C-x ( $x = 600, 700, 800, 900$  and 1000) can be decomposed into two components (Fig. 2e and Fig. S5). The major peak at around 284.7 eV corresponds to the C–C bond, which can significantly enhance the electrical conductivity of the WSe<sub>2</sub>/C supports [33,36]. The binding energy of the C–O bond located at around 287.0 eV indicates the presence of a small amount of oxygen-containing functional groups in the composites [33,36]. As shown in Fig. 2f and Fig. S6, two components can be observed by decomposing the O 1s peaks. The peak at around 530.8 eV corresponds to the W-bonded oxygen (O<sup>2-</sup>), indicating that the oxidization of W only happens on the subsurface of WSe<sub>2</sub>, consistent with the results of W 4f spectra [43]. The peak at around 532.7 eV is associated with the chemisorbed oxygen ions in the oxygen vacancy region [43].

### 3.2. Electrocatalytic activity analysis

To analysis the ORR activity and methanol tolerance property of Pt-WSe<sub>2</sub>/C, CV measurements are conducted in O<sub>2</sub>-saturated 0.5 M H<sub>2</sub>SO<sub>4</sub> solution with or without methanol (Fig. 3). Commercial Pt/C and WSe<sub>2</sub>/C are also used as the control samples. Compared with the individual WSe<sub>2</sub>/C and Pt/C, the improved reduction current density of the Pt-WSe<sub>2</sub>/C catalysts may be attributed to the increase of the number of exposed catalytic active-sites and the

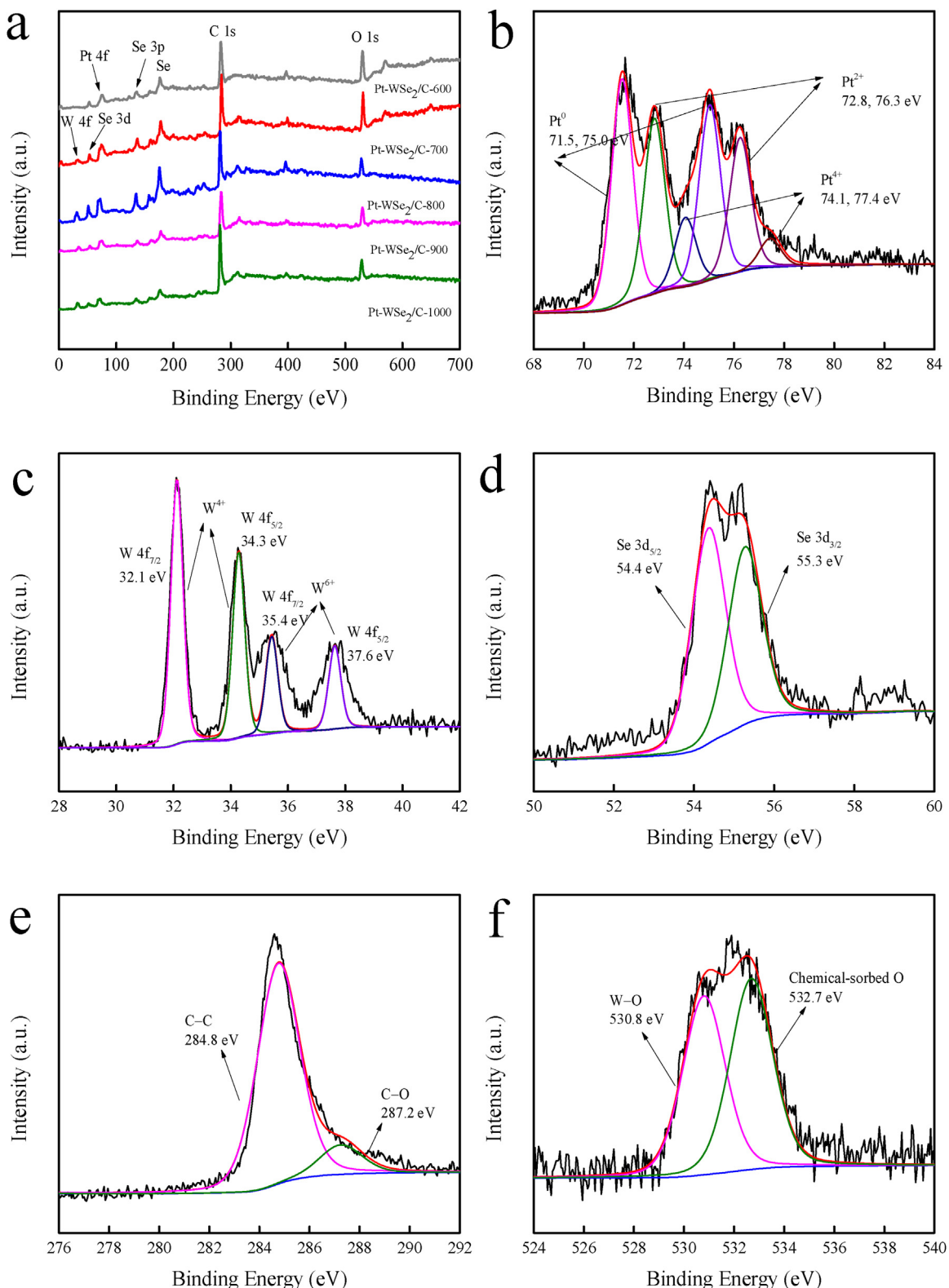


**Fig. 2.** XPS survey spectra (a) for Pt-WSe<sub>2</sub>/C-x (x = 600, 700, 800, 900 and 1000) and high resolution XPS of Pt 4f (b), W 4f (c), Se 3d (d), C 1s (e) and O 1s (f) for Pt-WSe<sub>2</sub>/C-800.

improved conductivity by offering easy transfer charge ability as an electrode (Table S2) [37]. Moreover, as shown in Fig. 3c, the anodic peak at  $-0.1$  V is attributed to hydrogen desorption on the Pt surface [29,44]. The presence of the small and broad anodic current peak is due to the adsorption of water-related species, such as hydroxyl species, which begins from  $0.1$  V and is amplified at  $0.6$  V

to result in the formation of Pt surface oxides and the adsorption of hydrogen on Pt [29,44]. The hydrogen desorption/adsorption peaks of the Pt-WSe<sub>2</sub>/C catalysts are completely suppressed, indicating that WSe<sub>2</sub>/C support can significantly modify the electrode surface. In addition, the Pt-WSe<sub>2</sub>/C-800 and Pt-WSe<sub>2</sub>/C-900 catalysts show the current density of  $4.57$  and  $4.01$   $\text{mA cm}^{-2}$ , respectively,

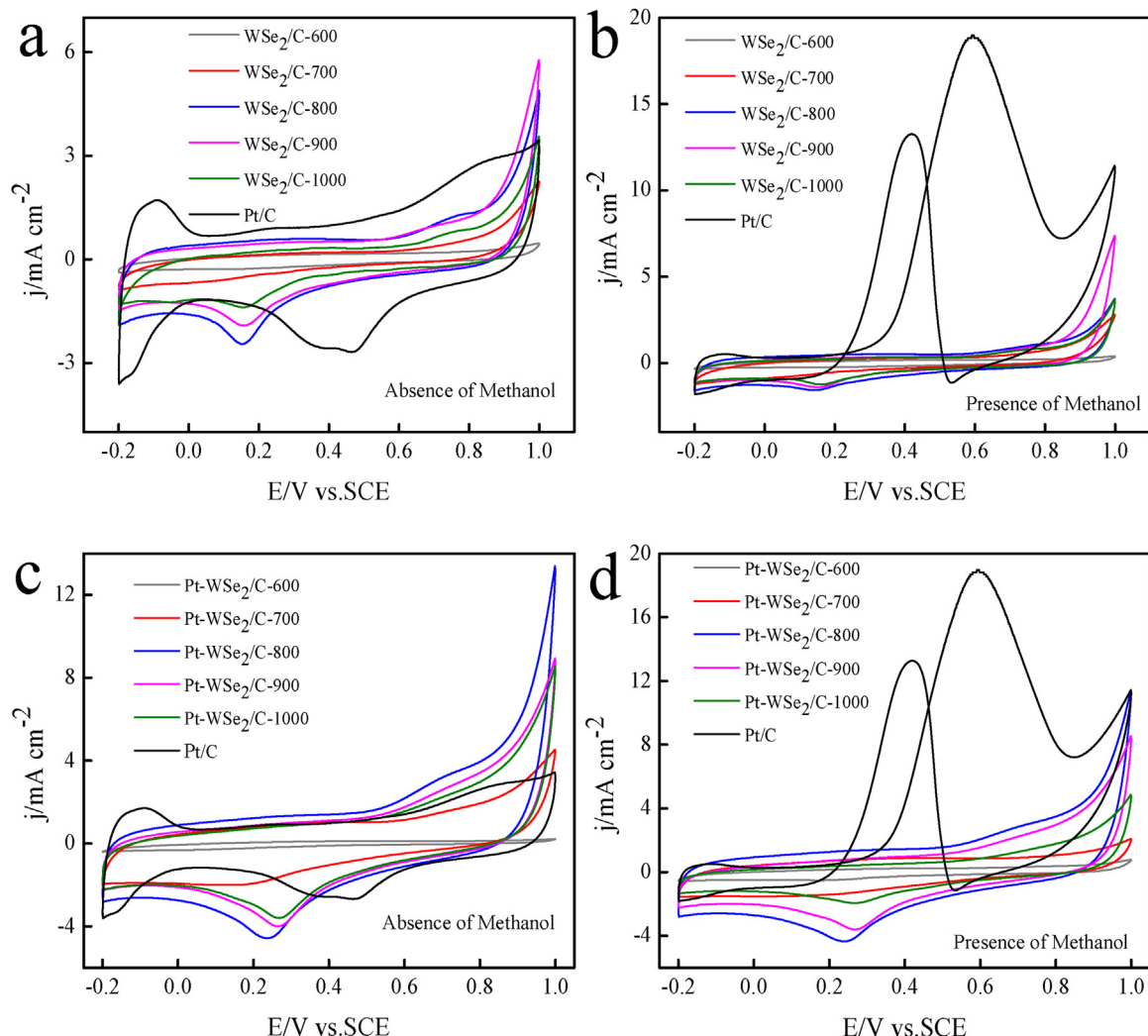


**Fig. 3.** CV curves of  $\text{WSe}_2/\text{C}$  (a) and  $\text{Pt}/\text{C}$  (b) in  $\text{O}_2$ -saturated  $0.5 \text{ M H}_2\text{SO}_4$  solution with or without  $0.5 \text{ M}$  methanol at a scan rate of  $10 \text{ mV s}^{-1}$ ; CV curves of  $\text{Pt-WSe}_2/\text{C}$  (c) and  $\text{Pt}/\text{C}$  (d) in  $\text{O}_2$ -saturated  $0.5 \text{ M H}_2\text{SO}_4$  solution with or without  $0.5 \text{ M}$  methanol at a scan rate of  $10 \text{ mV s}^{-1}$ .

which are higher than those of  $\text{Pt-WSe}_2/\text{C-1000}$  ( $3.61 \text{ mA cm}^{-2}$ ) and commercial  $\text{Pt}/\text{C}$  ( $2.69 \text{ mA cm}^{-2}$ ). There are no obvious reduction peaks for  $\text{Pt-WSe}_2/\text{C-600}$  and  $\text{Pt-WSe}_2/\text{C-700}$  catalysts because of the low crystallinity of  $\text{WSe}_2$ . Furthermore, the reduction peak of  $\text{Pt-WSe}_2/\text{C-800}$  has a slight negative shift, which can be attributed to the possible formation of a small amount of oxidized tungsten species [45]. The formed  $\text{WO}_x$ -species may slightly suppress the adsorption of new oxygen molecules on the  $\text{WSe}_2/\text{C}$  surface to reduce the ORR efficiency [45]. Fig. 3b and 3d show the CV curves of  $\text{WSe}_2/\text{C}$ ,  $\text{Pt-WSe}_2/\text{C}$  and  $\text{Pt}/\text{C}$  catalysts in methanolic acidic medium. The  $\text{Pt}/\text{C}$  exhibits a large methanol oxidation current peak at around  $0.6 \text{ V}$  in the positive scan direction, while the presence of methanol almost exerts no influence on the ORR activity of  $\text{WSe}_2/\text{C}$  and  $\text{Pt-WSe}_2/\text{C}$  catalysts, implying that the  $\text{WSe}_2/\text{C}$  and  $\text{Pt-WSe}_2/\text{C}$  catalysts are fully tolerant to the presence of methanol.

### 3.3. Detailed structure of $\text{Pt-WSe}_2/\text{C-x}$ ( $x = 800, 900$ ) and oxygen reduction kinetics

Because the performances of  $\text{Pt-WSe}_2/\text{C-x}$  ( $x = 800$  and  $900$ ) are better than those of other composites, their detailed structures are investigated (Fig. 4). SEM images of the  $\text{WSe}_2/\text{C-x}$  ( $x = 800$  and  $900$ ) and  $\text{Pt-WSe}_2/\text{C-x}$  ( $x = 800$  and  $900$ ) are shown in Fig. 4. As shown in Fig. 4a and 4b, some irregularly shaped particles can

be observed on the surface of carbon. Those particles are randomly distributed and some are stacked with each other. Moreover, some particles are aggregated to form huge agglomerates. The structure, surface functional groups and active surface area of the  $\text{WSe}_2/\text{C}$  supports/co-catalysts have a significant effect on the catalytic activity and durability of  $\text{Pt-WSe}_2/\text{C}$  catalysts. As shown in Fig. 4c, a large number of particles with relatively uniform diameters of approximately  $10\text{--}50 \text{ nm}$  are well dispersed on the surface of carbon skeleton and the stacking and agglomeration of the particles are efficiently alleviated, indicating that the use of  $\text{WSe}_2/\text{C-800}$  support can reduce the agglomeration tendency of Pt nanoparticles and increases the number of Pt active sites. As shown in Fig. 4d, there are a relatively small number of nanoparticles on the surface of  $\text{WSe}_2/\text{C-900}$ , which are tightly attached to the surface of carbon skeleton and/or  $\text{WSe}_2$ . As previously reported, the intimate contacts between the Pt particles and  $\text{WSe}_2/\text{C}$  skeleton can provide the robust and electrically conductive pathways, which are important for obtaining better catalytic activity.

Fig. 4e–j shows the TEM images of  $\text{Pt-WSe}_2/\text{C-800}$  and  $\text{Pt-WSe}_2/\text{C-900}$ . As shown in Fig. 4e, a large amount of nanoparticles with relatively homogeneous sizes and good dispersibility are tightly deposited on the carbon skeleton. While a small amount of nanoparticles with poor dispersibility can be seen from Fig. 4d, consistent with the results of SEM. Moreover, some smaller particles

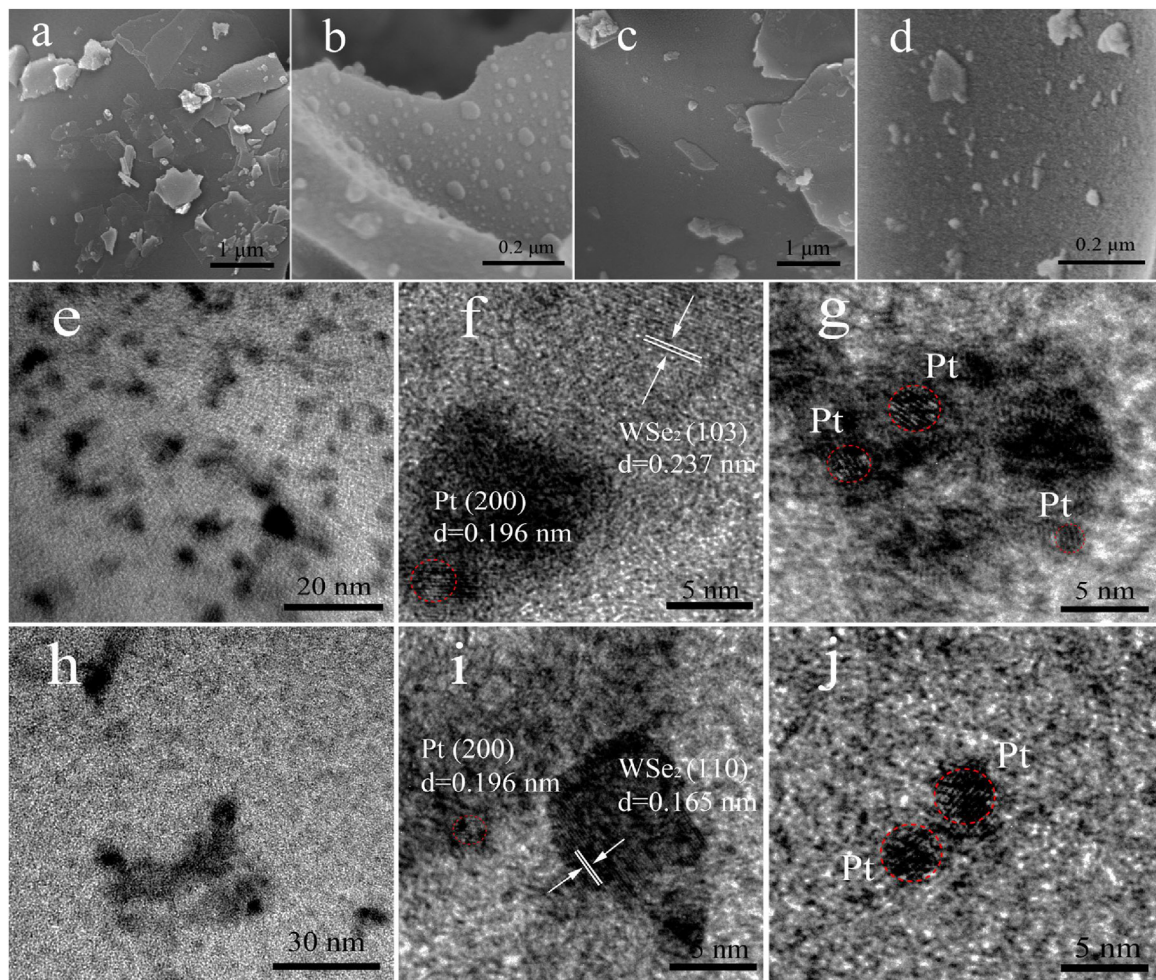


**Fig. 4.** SEM images of  $\text{WSe}_2/\text{C}-x$  ( $x=800$  (a) and  $900$  (b)) and  $\text{Pt}-\text{WSe}_2/\text{C}-x$  ( $x=800$  (c) and  $900$  (d)); TEM (e) and HRTEM (f and g) images of  $\text{Pt}-\text{WSe}_2/\text{C}-800$ ; TEM (h) and HRTEM (i and j) images of  $\text{Pt}-\text{WSe}_2/\text{C}-900$ .

(Pt) with better dispersion and less agglomeration can be observed on the surface of  $\text{Pt}-\text{WSe}_2/\text{C}-800$ , implying that more Pt active sites of  $\text{Pt}-\text{WSe}_2/\text{C}-800$  should be exposed [40]. In addition, the cross-linked network structure of  $\text{Pt}-\text{WSe}_2/\text{C}-800$  and  $\text{Pt}-\text{WSe}_2/\text{C}-900$  can enhance the oxygen permeation and electron transfer on the matrix [46]. In the HRTEM images (Fig. 4f and i),  $\text{WSe}_2$  and Pt are well crystallized in the carbon skeleton. As shown in Fig. 4g and j, the lattice spacing of  $0.196\text{ nm}$  is ascribed to the (200) plane of Pt. The lattice spacing of  $0.237$ ,  $0.165$  and  $0.196\text{ nm}$  correspond to the (103) and (110) planes of  $\text{WSe}_2$  and the (200) plane of Pt, respectively, which agrees with the XRD results. Furthermore, the Pt with (200) planes are mainly deposited in the vicinity of  $\text{WSe}_2$  to improve the charge transfer among Pt,  $\text{WSe}_2$  and C, which also can further use the co-catalytic effects of the exposed edge sites of  $\text{WSe}_2$  [40].

To compare the electron transfer resistance of reduction reaction and gain further insights on methanol tolerance properties, the EIS studies are performed and the Nyquist plots are obtained at peak potential of reduction at a frequency range of  $100\text{ kHz}$ – $100\text{ mHz}$  with the amplitude of the sine wave of  $5\text{ mV s}^{-1}$  in RDE (Fig. 5) [36,40]. The obtained charge transfer resistances ( $R_{\text{ct}}$ ) are shown in Table S3.  $\text{Pt}-\text{WSe}_2/\text{C}-800$  obtains the lowest  $R_{\text{ct}}$  of  $67.81\text{ }\Omega$ , which is lower than those of  $\text{Pt}/\text{C}$  ( $97.18\text{ }\Omega$ ) and  $\text{Pt}-\text{WSe}_2/\text{C}-900$  ( $108.1\text{ }\Omega$ ) in  $\text{O}_2$ -saturated acid electrolyte (methanol-free). It means that the fast electron transfer is occurred on the active sites of  $\text{Pt}-\text{WSe}_2/\text{C}-800$ . The highly uniform dispersion of Pt on the surface of  $\text{WSe}_2/\text{C}$  and the close integration between  $\text{WSe}_2/\text{C}$  and Pt can facilitate the

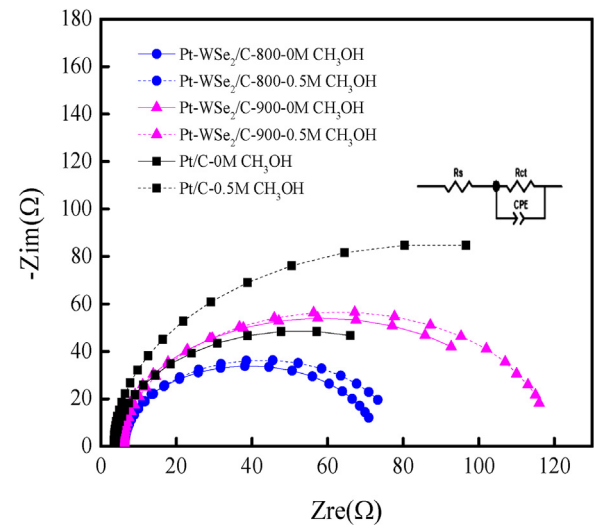


**Fig. 5.** Nyquist curves of the  $\text{Pt}-\text{WSe}_2/\text{C}-800$ ,  $\text{Pt}-\text{WSe}_2/\text{C}-900$  and  $\text{Pt}/\text{C}$  cathodes in  $\text{O}_2$ -saturated  $0.5\text{ M H}_2\text{SO}_4$  solution with and without  $0.5\text{ M}$  methanol at a scan rate of  $5\text{ mV s}^{-1}$  with an RDE rotation rate of  $1600\text{ rpm}$ .

exposure of more Pt active sites and the charge transfer kinetics [36,40]. In addition, the higher  $R_{\text{ct}}$  of  $\text{Pt}-\text{WSe}_2/\text{C}-900$  than that of  $\text{Pt}-\text{WSe}_2/\text{C}-800$  may be attributed to the random distribution of

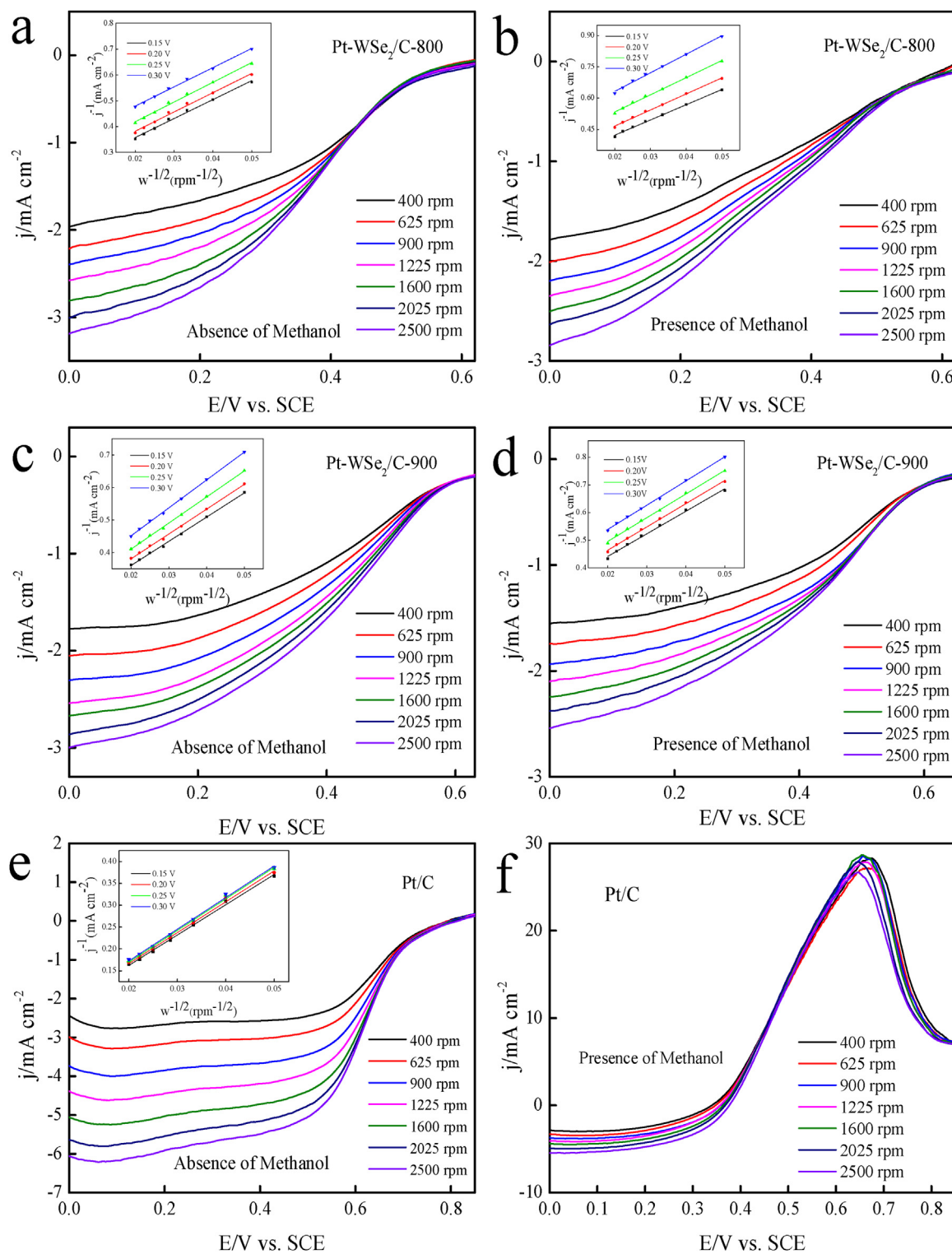


**Fig. 6.** Linear sweep voltammetry (LSV) and calculated K-L plots at different potentials (inset) of  $\text{Pt-WSe}_2/\text{C-800}$  (a and b),  $\text{Pt-WSe}_2/\text{C-900}$  (c and d) and  $\text{Pt/C}$  (e and f) in  $\text{O}_2$ -saturated  $0.5 \text{ M H}_2\text{SO}_4$  with or without  $0.5 \text{ M}$  methanol at a scan rate of  $5 \text{ mV s}^{-1}$  and at different RDE rotation rates.

Pt and the dilution and partial coverage of the ORR active sites on  $\text{Pt-WSe}_2/\text{C-900}$ , which can inhibit the fast flow of electrons [47]. Commercial  $\text{Pt/C}$  catalyst exhibits a far higher  $R_{\text{ct}}$  increase (75.03%) in the presence of  $0.5 \text{ M}$  methanol, implying that the  $\text{Pt-WSe}_2/\text{C-800}$  (increase of 7.25%) and  $\text{Pt-WSe}_2/\text{C-900}$  (increase of 2.96%) catalysts have much better methanol tolerance than that of  $\text{Pt/C}$ . Methanol tolerance is a specific nature for  $\text{Pt-WSe}_2/\text{C}$  catalysts, which should originate from the co-catalytic/protective roles

of  $\text{WSe}_2$  embedded in the carbon skeleton to compromise the methanol cross-over poisoning effect.

The RDE tests, which are carried out in  $\text{O}_2$ -saturated  $0.5 \text{ M H}_2\text{SO}_4$  solution with or without  $0.5 \text{ M}$  methanol at a scan rate of  $5 \text{ mV s}^{-1}$ , are employed to explore the ORR kinetics and electron transfer number ( $n$ ) of the catalysts [33]. As shown in Fig. 6, the diffusion current densities increase with the increasing rotating rates by shortening the diffusion distance at high speeds. All of the K-L

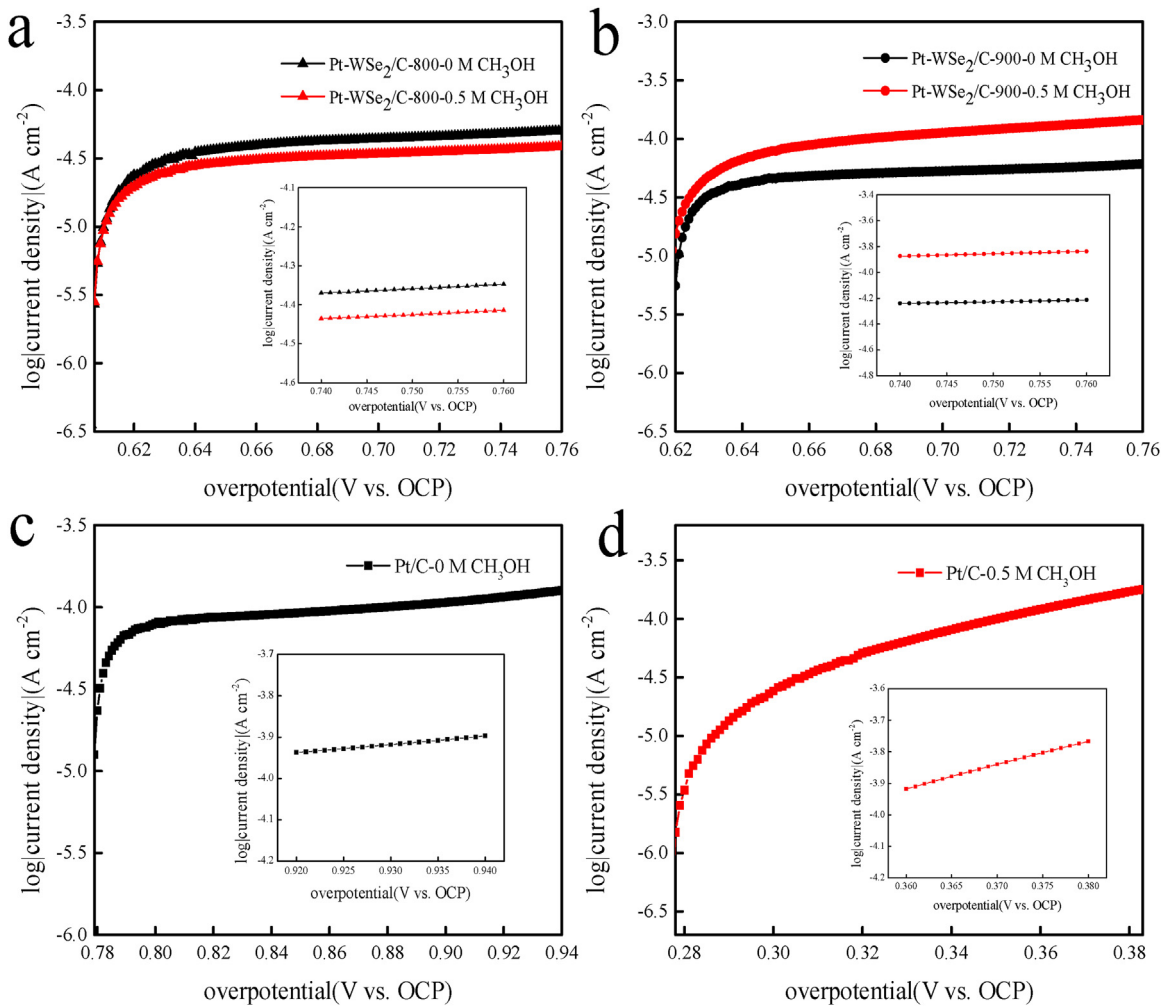


**Fig. 7.** Tafel plots of the Pt-WSe<sub>2</sub>/C-800 (a) and Pt-WSe<sub>2</sub>/C-900 (b) catalysts compared with Pt/C in the absence (c) and presence (d) of methanol.

plots display good linearity at different potentials from 0.15 to 0.3 V, suggesting that the first-order reaction kinetics toward the ORR is conducted on Pt-WSe<sub>2</sub>/C-800, Pt-WSe<sub>2</sub>/C-900 and Pt/C. The electron transfer number per oxygen molecule (n) involved in oxygen reduction is calculated from the slopes of K-L plots (Fig. S7) [33]. In the absence of methanol, the n values of Pt-WSe<sub>2</sub>/C-800 (3.84), Pt-WSe<sub>2</sub>/C-900 (3.86) and Pt/C (4.05) are close to the theoretically calculated value (n = 4.0) at a limiting potential of 0.15 V, indicating that their dominant pathways for ORR are the 4 e<sup>-</sup> oxygen reduction [33]. Although the n values decrease with the increase of the potential, it mainly favors a 4e<sup>-</sup> oxygen reduction process. In addition, the more exposed Pt active sites on Pt-WSe<sub>2</sub>/C can contribute to the fast adsorption and activation of oxygen molecules during the ORR. In the presence of 0.5 M methanol, the polarization diagrams for ORR on the Pt/C electrode have changed obviously (Fig. 6f). The Pt/C exhibits a large anodic current at around 0.6 V because of the oxidation of methanol on Pt/C catalyst, whereas no appreciable anodic current is detected for Pt-WSe<sub>2</sub>/C catalysts (Fig. 6b and 6d), implying that the methanol tolerance and ORR selectivity of Pt-WSe<sub>2</sub>/C-x (800 and 900) are significantly higher than those of Pt/C [29].

Moreover, 0.5 M methanol causes a 150 mV negative shift in half-wave potential of Pt/C catalyst at a rotating rate of 1600 rpm due to the formation of a mixed potential, which is caused by the simultaneous reactions of the methanol oxidation (MOR) and oxygen reduction on the surface of Pt/C catalyst [38,48]. These results clearly suggest that commercial Pt/C has no methanol tolerance

and such a mixed potential at the cathode should negatively affect the cathode performance of the DMFCs [29]. For Pt-WSe<sub>2</sub>/C-800 and Pt-WSe<sub>2</sub>/C-900, there are only 10 and 15 mV negative shifts in half-wave potential, illustrating their much stronger methanol tolerance properties. In the presence of methanol, the ORR onset potentials of the Pt-WSe<sub>2</sub>/C-800 and Pt-WSe<sub>2</sub>/C-900 at 1600 rpm are 0.55 and 0.58 V, respectively, both of which are much higher than that of Pt/C (0.40 V), demonstrating that Pt-WSe<sub>2</sub>/C catalysts have higher ORR activity than that of Pt/C [49]. Furthermore, Pt-WSe<sub>2</sub>/C-900 affords slightly higher onset potential (activity) than that of Pt-WSe<sub>2</sub>/C-800, which can be attributed to the better synergistic effects between the sufficient exposed edge sites of well-crystallized WSe<sub>2</sub> and the highly conductive carbon skeleton with abundant oxygen-containing functional groups. These results suggest that Pt-WSe<sub>2</sub>/C-800 and Pt-WSe<sub>2</sub>/C-900 catalysts can be considered as promising ORR catalysts for DMFCs cathode.

Fig. 7 shows the tafel plots for Pt-WSe<sub>2</sub>/C-800, Pt-WSe<sub>2</sub>/C-900 and Pt/C in O<sub>2</sub>-saturated 0.5 M H<sub>2</sub>SO<sub>4</sub> solution with or without methanol at a rotating rate of 1600 rpm. The exchange current density ( $j_0$ ), which is related to the concentration of the reactants and the active free energy at the equilibrium potential, is used to evaluate the ORR performance (Table 2) [46]. As shown in Table S2, the exchange current density of Pt/C drastically changes from  $1.62 \times 10^{-6}$  (without methanol) to  $2.32 \times 10^{-7}$  (0.5 M methanol), which can be related to the relative coverage of methanolic/oxygen adsorbed species on the surface of Pt [12]. The  $j_0$  values for Pt-WSe<sub>2</sub>/C-800 and Pt-WSe<sub>2</sub>/C-900 electrodes are slightly affected by

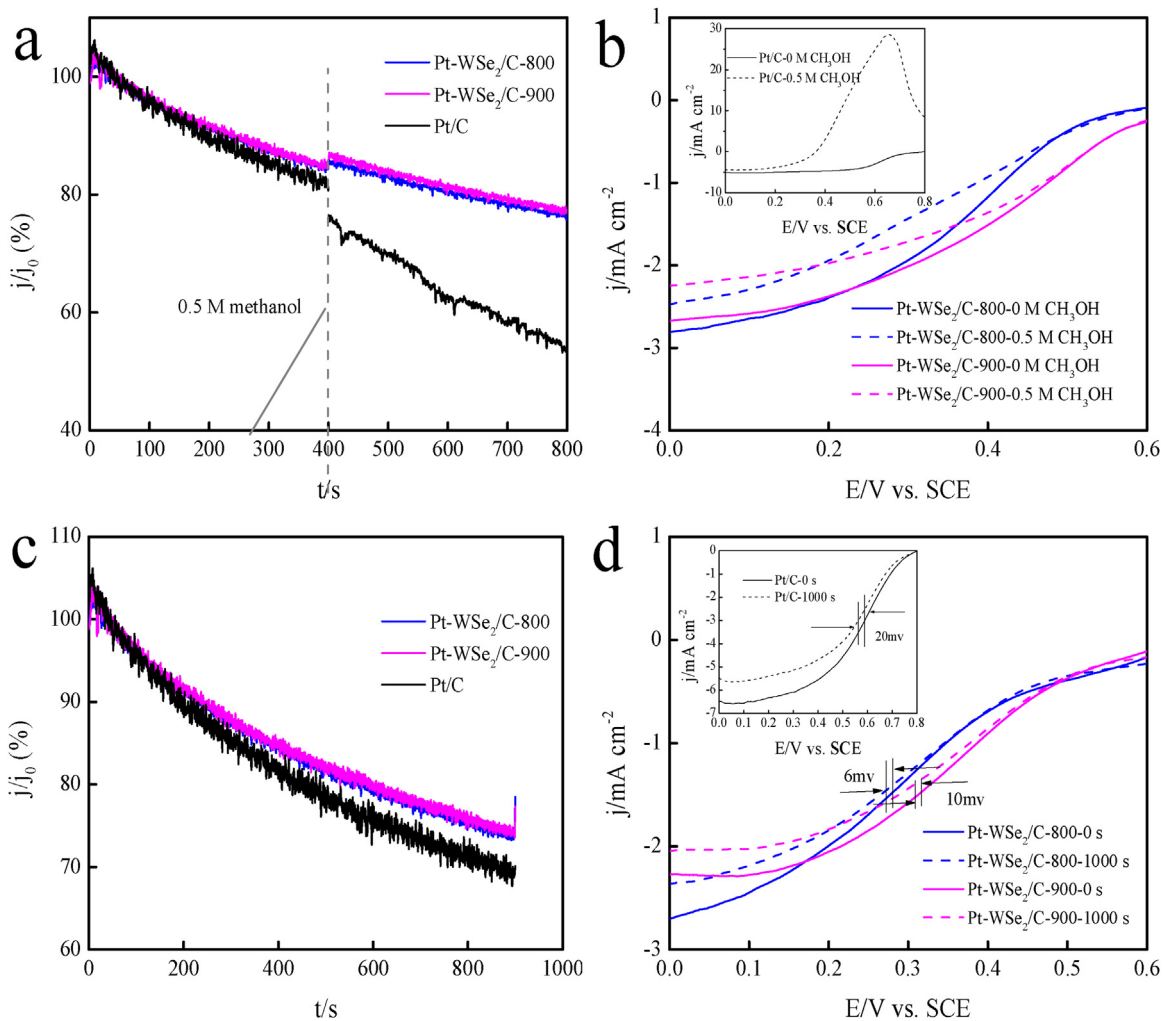


**Fig. 8.** Chronoamperometric (a) and ORR polarization curves (b) of Pt-WSe<sub>2</sub>/C-800, Pt-WSe<sub>2</sub>/C-900 and Pt/C before and after the addition of 0.5 M methanol in an O<sub>2</sub>-saturated 0.5 M H<sub>2</sub>SO<sub>4</sub> at 1600 rpm; (c) Chronoamperometric curves of Pt-WSe<sub>2</sub>/C-800, Pt-WSe<sub>2</sub>/C-900 and Pt/C at a rotation rate of 1600 rpm in an O<sub>2</sub>-saturated 0.5 M H<sub>2</sub>SO<sub>4</sub> solution; (d) ORR polarization curves of Pt-WSe<sub>2</sub>/C-800, Pt-WSe<sub>2</sub>/C-900 and Pt/C before and after the continuous operation for 1000 s in an O<sub>2</sub>-saturated 0.5 M H<sub>2</sub>SO<sub>4</sub> solution at 1600 rpm.

**Table 2**  
Linear fit equations and exchange current densities (j<sub>0</sub>) of the Tafel plots.

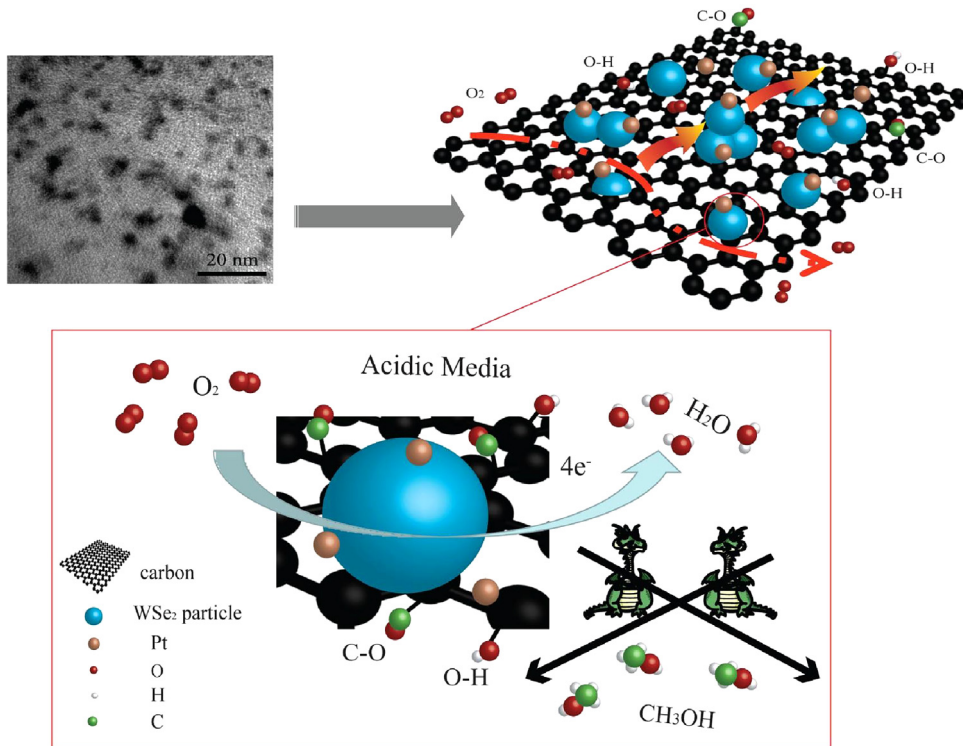
Samples	Fit linear equation	(R <sup>2</sup> )	j <sub>0</sub> (A cm <sup>-2</sup> )
Pt-WSe <sub>2</sub> /C-800 (0 M CH <sub>3</sub> OH)	y = 1.157 × -5.177	0.999	6.65 × 10 <sup>-6</sup>
Pt-WSe <sub>2</sub> /C-800 (0.5 M CH <sub>3</sub> OH)	y = 1.060 × -5.220	0.998	6.03 × 10 <sup>-6</sup>
Pt-WSe <sub>2</sub> /C-900 (0 M CH <sub>3</sub> OH)	y = 1.333 × -5.227	0.997	5.93 × 10 <sup>-6</sup>
Pt-WSe <sub>2</sub> /C-900 (0.5 M CH <sub>3</sub> OH)	y = 1.870 × -5.259	0.999	5.51 × 10 <sup>-6</sup>
Pt/C (0 M CH <sub>3</sub> OH)	y = 2.014 × -5.791	0.999	1.62 × 10 <sup>-6</sup>
Pt/C (0.5 M CH <sub>3</sub> OH)	y = 7.551 × -6.635	0.999	2.32 × 10 <sup>-7</sup>

the presence of methanol, indicating the high methanol tolerance of both catalysts. Furthermore, their j<sub>0</sub> values are far higher than that of Pt/C, implying that the ORR performance of Pt-WSe<sub>2</sub>/C-800 and Pt-WSe<sub>2</sub>/C-900 should be better than that of Pt/C [46].

The good durability and tolerance to methanol crossover are the important properties for catalysts in DMFCs. Fig. 8a shows the chronoamperometric responses of Pt-WSe<sub>2</sub>/C-800, Pt-WSe<sub>2</sub>/C-900 and Pt/C catalysts for ORR with the injection of 0.5 M methanol into the O<sub>2</sub>-saturated 0.5 M H<sub>2</sub>SO<sub>4</sub> electrolyte. A sharp decrease of the retention ratio of the current can be observed for commercial Pt/C with 0.5 M methanol, while the Pt-WSe<sub>2</sub>/C-800 and Pt-WSe<sub>2</sub>/C-900 electrodes are insensitive to methanol. The little change of the ORR polarization curves for Pt-WSe<sub>2</sub>/C-800 and Pt-WSe<sub>2</sub>/C-900 catalysts before and after the addition of 0.5 M methanol suggests

that Pt-WSe<sub>2</sub>/C-x (800 and 900) catalysts have a strong tolerance to methanol crossover (Fig. 8b). As shown in Fig. 8c, the cycling durability of Pt-WSe<sub>2</sub>/C-x (800 and 900) catalysts for ORR is investigated by chronoamperometric measurements at the peak potential in an O<sub>2</sub>-saturated 0.5 M H<sub>2</sub>SO<sub>4</sub> electrolyte. The current densities of all of the electrodes gradually decrease with time. However, the Pt-WSe<sub>2</sub>/C-800 and Pt-WSe<sub>2</sub>/C-900 electrodes exhibit slower decay rates by maintaining 78.5 and 77.4% of their initial current densities after 1000 s, respectively, which are higher than that of the commercial Pt/C electrode (70.1%). Furthermore, the half-wave potentials for Pt-WSe<sub>2</sub>/C-800 and Pt-WSe<sub>2</sub>/C-900 electrodes in the ORR polarization curves negatively shift only 6 and 10 mV, respectively, while there is up to 20 mV negative shift for Pt/C after the continuous operation over 1000 s (Fig. 8d). The higher durability of Pt-WSe<sub>2</sub>/C-800 and Pt-WSe<sub>2</sub>/C-900 are mainly attributed to the strong interaction among WSe<sub>2</sub>, Pt and carbon, which can inhibit the self-aggregation of metallic Pt during the catalytic process to remain the available number of the catalytically active sites on the catalyst surface [1,33]. These results indicate that Pt-WSe<sub>2</sub>/C-800 and Pt-WSe<sub>2</sub>/C-900 possess better ORR activity and durability than those of commercial Pt/C. Hence, WSe<sub>2</sub>/C can be considered as a promising Pt-support/electrocatalyst for ORR in fuel cells.

Through the above analyses, the process and mechanism of oxygen reduction reaction are shown in Scheme 1. Compared with



**Scheme 1.** Schematic diagram of oxygen reduction reaction processes on Pt-WSe<sub>2</sub>/C catalysts.

bare WSe<sub>2</sub> and commercial Pt/C, the improved activity of the Pt-WSe<sub>2</sub>/C catalysts may be attributed to three aspects: (1) the WSe<sub>2</sub> nanoparticles are in situ embedded in the carbon skeleton, meanwhile Pt nanoparticles are well-dispersed on the surface of WSe<sub>2</sub>/C, which can effectively reduce the Pt self-aggregation during the catalytic process and thus prevent the loss of active sites to maximally expose the active-sites; (2) the robust contact among Pt, WSe<sub>2</sub> and carbon can promote the efficiently electrical communication between the catalytic edge-sites and the underlying carbon skeleton, thereby improving the charge transfer efficiency; (3) the porous structure of Pt-WSe<sub>2</sub>/C catalyst is also conducive to the permeation, diffusion and transport of O<sub>2</sub>, which energetically contribute to the fast adsorption, activation and reduction of oxygen molecules during the ORR. In addition, the diffusion of methanol molecules from the aqueous solution to the catalyst layer has no harmful effect on the reaction among oxygen molecules, electrons and protons, which are mainly participated in the ORR process to generate water molecules. As a result, the as-prepared Pt-WSe<sub>2</sub>/C catalysts exhibit the promising ORR activity and methanol tolerance.

#### 4. Conclusions

In summary, we present a facile synthetic route to synthesize Pt-WSe<sub>2</sub>/C as a highly active, durable and methanol-tolerant electrocatalyst for ORR in DMFCs. The specific surface area and electrical conductivity of WSe<sub>2</sub>/C are controlled by tuning the carbonization temperature (600–1000 °C). The synthesized Pt-WSe<sub>2</sub>/C-800 catalyst exhibits the highest current density (4.57 mA cm<sup>-2</sup>) in acidic medium, which is better than that of commercial Pt/C (10 wt.%) as determined by CV tests. Pt-WSe<sub>2</sub>/C-800 also exhibits the higher tolerance to methanol crossover and the longer-term durability than those of Pt/C catalyst. The *n* value for ORR on the Pt-WSe<sub>2</sub>/C-800 catalyst is 3.84, indicating that a 4e<sup>-</sup> reduction pathway is favored and similar to commercial Pt/C catalyst. The highly efficient active sites composed of uniform distribution of WSe<sub>2</sub> and deposited Pt

nanocrystals on the carbon skeleton, the high BET surface area, and the good electrical conductivity can synergistically improve the ORR activity and reduce the R<sub>ct</sub>. It also demonstrates that the fast electron transport characteristics and the high density of active sites play the important roles in determining the catalytic performance and structure-activity correlations of Pt-WSe<sub>2</sub>/C. Hence, this study provides new insights for the potential application of WSe<sub>2</sub>/C as high-activity and strong methanol-tolerance cathode catalyst/support with low-cost in DMFCs.

#### Acknowledgments

We acknowledge the support by National Natural Science Foundation of China (51578218, 51108162, 21473051), Natural Science Foundation of Heilongjiang Province (QC2015009), Postdoctoral Science Foundation of Heilongjiang Province (LBH-Q14137), Scientific and technological innovation talents of Harbin (2016RQQXJ119), and Excellent Young Teachers Fund of Heilongjiang University and Hundred Young Talents in Heilongjiang University.

#### Appendix A. Supplementary data

Supplementary data associated with this article can be found, in the online version, at <http://dx.doi.org/10.1016/j.apcatb.2017.07.011>.

#### References

- [1] J. Xiao, Y. Xu, Y. Xia, J. Xi, S. Wang, Ultra-small Fe<sub>2</sub>N nanocrystals embedded into mesoporous nitrogen-doped graphitic carbon spheres as a highly active, stable and methanol-tolerant electrocatalyst for the oxygen reduction reaction, *Nano Energy* 24 (2016) 121–129.
- [2] Y. Tan, C. Xu, G. Chen, N. Zheng, J.Q. Xie, A graphene-platinum nanoparticles-ionic liquid composite catalyst for methanol-tolerant oxygen reduction reaction, *Energy Environ. Sci.* 5 (2012) 6923–6927.
- [3] J.S. Li, H.Q. Dong, S.L. Li, R.H. Li, Z.H. Dai, J.C. Bao, Y.Q. Lan, Polyoxometalate-assisted fabrication of the Pd nanoparticle/reduced

graphene oxide nanocomposite with enhanced methanol-tolerance for the oxygen reduction reaction, *New J. Chem.* 40 (2016) 914–918.

[4] J. Ma, D. Ai, X. Xie, J. Guo, Novel methanol-tolerant Ir-S/C chalcogenide electrocatalysts for oxygen reduction in DMFC fuel cell, *Particuology* 9 (2011) 155–160.

[5] L. Lu, R. Li, K. Fujiwara, X. Yan, H. Kobayashi, W. Yi, J. Fan, Cyanide radical chemisorbed Pt electrocatalyst for enhanced methanol-Tolerant oxygen reduction reactions, *J. Phys. Chem. C* 120 (2016) 11572–11580.

[6] C. Si, J. Zhang, Y. Wang, W. Ma, H. Gao, L. Lv, Z. Zhang, Nanoporous Platinum/(Mn,Al)<sub>3</sub>O<sub>4</sub> nanosheet nanocomposites with synergistically enhanced ultrahigh oxygen reduction activity and excellent methanol tolerance, *ACS Appl. Mater. Interfaces* 9 (2017) 2485–2494.

[7] M.R. Gao, J. Jiang, S.H. Yu, Solution-based synthesis and design of late transition metal chalcogenide materials for oxygen reduction reaction (ORR), *Small* 8 (2012) 13–27.

[8] Y. Feng, A. Gago, L. Timperman, N. Alonso-Vante, Chalcogenide metal centers for oxygen reduction reaction: activity and tolerance, *Electrochim. Acta* 56 (2011) 1009–1022.

[9] Z. Chen, D. Higgins, A. Yu, L. Zhang, J. Zhang, A review on non-precious metal electrocatalysts for PEM fuel cells, *Energy Environ. Sci.* 4 (2011) 3167–3192.

[10] R. Cao, J. Lee, M. Liu, J. Cho, Recent progress in non-precious catalysts for metal-air batteries, *Adv. Energy Mater.* 2 (2012) 816–829.

[11] J. Masud, M. Nath, Co<sub>7</sub>Se<sub>8</sub> nanostructures as catalysts for oxygen reduction reaction with high methanol tolerance, *ACS Energy Lett.* 1 (2016) 27–31.

[12] D. Sebastian, A. Serov, K. Artyushkova, P. Atanassov, A.S. Arico, V. Baglio, Performance, methanol tolerance and stability of Fe-aminobenzimidazole derived catalyst for direct methanol fuel cells, *J. Power Sources* 319 (2016) 235–246.

[13] A. Swesi, J. Masud, M. Nath, Nickel selenide as high-efficiency catalyst for oxygen evolution reaction, *Energy Environ. Sci.* 9 (2016) 1771–1782.

[14] K. Suárez-Alcántara, A. Ezeta-Mejía, M. Ortega-Avilés, D. Haase, E. Arce-Estrada, R.G. Gonzalez-Huerta, O. Solorza-Feria, S.E. Canton, Synchrotron-based structural and spectroscopic studies of ball milled RuSeMo and RuSnMo particles oxygen reduction electrocatalyst for PEM fuel cells, *Int. J. Hydrogen Energy* 39 (2014) 16715–16721.

[15] K.T. Jeng, N.Y. Hsu, C.C. Chien, Synthesis and evaluation of carbon nanotube-supported RuSe catalyst for direct methanol fuel cell cathode, *Int. J. Hydrogen Energy* 36 (2011) 3997–4006.

[16] F.S. Zheng, S.H. Liu, C.W. Kuo, Ultralow Pt amount of PteFe alloys supported on ordered mesoporous carbons with excellent methanol tolerance during oxygen reduction reaction, *Int. J. Hydrogen Energy* 41 (2016) 2487–2497.

[17] S. Takahashi, N. Takahashi, N. Todoroki, T. Wadayama, Dealloying of nitrogen-Introduced Pt–Co alloy nanoparticles: preferential core–Shell formation with enhanced activity for oxygen reduction reaction, *ACS Omega* 1 (2016) 1247–1252.

[18] N. Jung, Y. Sohn, H.P. Jin, K.S. Nahm, P. Kim, S.J. Yoo, High-performance PtCu@Pt core–shell nanoparticles decorated with nanoporous Pt surfaces for oxygen reduction reaction, *Appl. Catal. B: Environ.* 196 (2016) 199–206.

[19] T.Y. Jeon, S.K. Kim, N. Pinna, A. Sharma, J. Park, S.Y. Lee, H.C. Lee, S.W. Kang, H.K. Lee, H.H. Lee, Selective dissolution of surface nickel close to platinum in PtNi nanocatalyst toward oxygen reduction reaction, *Chem. Mater.* 28 (2016) 1879–1887.

[20] N.E. Sahin, T.W. Napporn, L. Dubau, F. Kadirgan, J.M. Leger, K.B. Kokoh, Temperature-dependence of oxygen reduction activity on Pt/C and PtCr/C electrocatalysts synthesized from microwave-heated diethylene glycol method, *Appl. Catal. B: Environ.* 203 (2017) 72–84.

[21] S. Xie, S.I. Choi, N. Lu, L.T. Roling, J.A. Herron, L. Zhang, J. Park, J. Wang, M.J. Kim, Z.X. Xie, M. Mavrikakis, Y. Xia, Atomic layer-by-layer deposition of Pt on Pd nanocubes for catalysts with enhanced activity and durability toward oxygen reduction, *Nano Lett.* 14 (2014) 3570–3576.

[22] Y. Dai, S.G. Chen, Oxygen reduction electrocatalyst of Pt on Au nanoparticles through spontaneous deposition, *ACS Appl. Mater. Interfaces* 7 (2015) 823–829.

[23] M. Sun, H.J. Liu, Y. Liu, J.H. Qu, J.H. Li, Graphene-based transition metal oxide nanocomposites for the oxygen reduction reaction, *Nanoscale* 7 (2015) 1250–1269.

[24] Y. Wang, G. Li, J.H. Jin, S.L. Yang, Hollow porous carbon nanofibers as novel support for platinum-based oxygen reduction reaction electrocatalysts, *Int. J. Hydrogen Energy* 42 (2017) 5938–5947.

[25] Y. Chen, J. Xu, X. Liu, Y. Tang, T. Lu, Electrostatic self-assembly of platinum nanochains on carbon nanotubes: a highly active electrocatalyst for the oxygen reduction reaction, *Appl. Catal. B: Environ.* 140–141 (2013) 552–558.

[26] C. Zhu, S. Dong, Recent progress in graphene-based nanomaterials as advanced electrocatalysts towards oxygen reduction reaction, *Nanoscale* 5 (2013) 1753–1767.

[27] M. Stojmenovic, M. Momcilovic, N. Gavrilov, I.A. Pašti, S. Mentus, B. Jokic, B. Babic, Incorporation of Pt, Ru and Pt–Ru nanoparticles into ordered mesoporous carbons for efficient oxygen reduction reaction in alkaline media, *Electrochim. Acta* 153 (2015) 130–139.

[28] W. Song, Z. Chen, C. Yang, Z. Yang, J. Tai, Y. Nan, H. Lu, Carbon-coated, methanol-tolerant platinum/graphene catalysts for oxygen reduction reaction with excellent long-term performance, *J. Mater. Chem. A* 3 (2015) 1049–1057.

[29] R.F. Wang, S.J. Liao, H.Y. Liu, H. Meng, Synthesis and characterization of Pt–Se/C electrocatalyst for oxygen reduction and its tolerance to methanol, *J. Power Sources* 171 (2007) 471–476.

[30] M.L. Zou, J.D. Chen, L.F. Xiao, H. Zhu, T.T. Yang, M. Zhang, M.L. Du, WSe<sub>2</sub> and W(Se<sub>x</sub>S<sub>1-x</sub>)<sub>2</sub> nanoflakes grown on carbon nanofibers for the electrocatalytic hydrogen evolution reaction, *J. Mater. Chem. A* 3 (2015) 18090–18097.

[31] X. Wang, Y. Chen, B. Zheng, F. Qi, J. He, Q. Li, P. Li, W. Zhang, Graphene-like WSe<sub>2</sub> nanosheets for efficient and stable hydrogen evolution, *J. Alloys Compd.* 691 (2017) 698–704.

[32] Y. Sun, X. Zhang, B. Mao, M. Cao, Controllable selenium vacancy engineering in basal planes of mechanically exfoliated WSe<sub>2</sub> monolayer nanosheets for efficient electrocatalytic hydrogen evolution, *Chem. Commun.* 52 (2016) 14266–14269.

[33] J. Guo, Y. Shi, X. Bai, X. Wang, T. Ma, Atomically thin MoSe<sub>2</sub>/graphene and WSe<sub>2</sub>/graphene nanosheets for the highly efficient oxygen reduction reaction, *J. Mater. Chem. A* 3 (2015) 24397–24404.

[34] M.L. Zou, J.F. Zhang, H. Zhu, M.L. Du, Q.F. Wang, M. Zhang, X. Zhang, A 3D dendritic WSe<sub>2</sub> catalyst grown on carbon nanofiber mats for efficient hydrogen evolution, *J. Mater. Chem. A* 3 (2015) 12149–12153.

[35] Z. Liu, H. Zhao, N. Li, Y. Zhang, X. Zhang, Y. Du, Assembled 3D electrocatalysts for efficient hydrogen evolution: wSe<sub>2</sub> layers anchored on graphene sheets, *Inorg. Chem. Front.* 3 (2016) 313–319.

[36] X. Wang, Y. Chen, F. Qi, B. Zheng, J. He, Q. Li, P. Li, W. Zhang, Y. Li, Interwoven WSe<sub>2</sub>/CNTs hybrid network: a highly efficient and stable electrocatalyst for hydrogen evolution, *Electrochim. Commun.* 72 (2016) 74–78.

[37] R. Li, Y. Dai, B. Chen, J. Zou, B.J. Jiang, H. Fu, Nitrogen-doped Co/Co<sub>9</sub>S<sub>8</sub>/partly-graphitized carbon as durable catalysts for oxygen reduction in microbial fuel cells, *J. Power Sources* 307 (2016) 1–10.

[38] E. Meku, C. Du, Y. Wang, L. Du, Y. Sun, F. Kong, G. Yin, Concentration gradient Pd–Ir–Ni/C electrocatalyst with enhanced activity and methanol tolerance for oxygen reduction reaction in acidic medium, *Electrochim. Acta* 192 (2016) 177–187.

[39] I.S. Park, O.H. Kim, J.W. Kim, B. Choi, Y.H. Cho, Y.E. Sung, Synthesis of Pt and bimetallic PtPd nanostructures on Au nanoparticles for use as methanol tolerant oxygen reduction reaction catalysts, *New J. Chem.* 39 (2015) 6034–6039.

[40] Y. Duan, Y. Sun, L. Wang, Y. Dai, B. Chen, S. Pan, J. Zou, Enhanced methanol oxidation and CO tolerance using oxygen-passivated molybdenum phosphide/carbon supported Pt catalysts, *J. Mater. Chem. A* 4 (2016) 7674–7682.

[41] Y. Duan, Y. Sun, S. Pan, Y. Dai, L. Hao, J. Zou, Self-Stable WP/C support with excellent cocatalytic functionality for Pt: enhanced catalytic activity and durability for methanol electro-Oxidation, *ACS Appl. Mater. Interfaces* 8 (2016) 33572–33582.

[42] Z.B. Wang, C.Z. Li, D.M. Gu, G.P. Yin, Carbon riveted PtRu/C catalyst from glucose in-suit carbonization through hydrothermal method for direct methanol fuel cell, *J. Power Sources* 238 (2013) 283–289.

[43] B. Yu, Z. Zheng, X. Wang, F. Qi, J. He, W. Zhang, Y. Chen, Enhanced photocatalytic properties of graphene modified few-layered WSe<sub>2</sub> nanosheets, *Appl. Surf. Sci.* 400 (2017) 420–425.

[44] A. Esfandiari, M. Kazemeini, D. Bastani, Synthesis, characterization and performance determination of an Ag@Pt/C electrocatalyst for the ORR in a PEM fuel cell, *Int. J. Hydrogen Energy* 41 (2016) 20720–20730.

[45] F. Fouda-Onana, S. Bah, O. Savadogo, Palladium-copper alloys as catalysts for the oxygen reduction reaction in an acidic media I: Correlation between the ORR kinetic parameters and intrinsic physical properties of the alloys, *J. Electroanal. Chem.* 639 (2009) 1–9.

[46] L. Hao, J. Yu, X. Xu, L. Yang, Z. Xing, Y. Dai, Y. Sun, J. Zou, Nitrogen-doped Mo<sub>2</sub>/carbon as highly oxygen-permeable and stable catalysts for oxygen reduction reaction in microbial fuel cells, *J. Power Sources* 339 (2017) 68–79.

[47] H. Gharibi, M. Amani, H. Pahlavanzadeh, M. Kazemeini, Investigation of carbon monoxide tolerance of platinum nanoparticles in the presence of optimum ratio of doped polyaniline with para toluene sulfonic acid and their utilization in a real passive direct methanol fuel cell, *Electrochim. Acta* 97 (2013) 216–225.

[48] D. Wu, D. Cheng, Core/shell AgNi/PtAgNi nanoparticles as methanol-tolerant oxygen reduction electrocatalysts, *Electrochim. Acta* 180 (2015) 316–322.

[49] K. Lee, L. Zhang, J. Zhang, A novel methanol-tolerant Ir–Se chalcogenide electrocatalyst for oxygen reduction, *J. Power Sources* 165 (2007) 108–113.